PERGAMON

International Journal of Heat and Mass Transfer 42 (1999) 1023–1036

International Journal of HEAT and MASS TRANSFER

Characteristics of flow instabilities from unstable stratification of density in channel shear layers at low Reynolds numbers

Supriya Gupta[a,b], Phillip M. Ligrani[c,*], J. Calvin Giddings[a]

[a] *Field-Flow Fractionation Research Center, Department of Chemistry*
[b] *Department of Chemical and Fuels Engineering*
[c] *Convective Heat Transfer Laboratory, Department of Mechanical Engineering, University of Utah, Salt Lake City, UT 84112, U.S.A.*

Received 12 September 1997; in final form 2 May 1998

Abstract

The instabilities which form due to globally unstable stratification of density in the shear layer which develops between two coincident streams of different velocity in a channel are described. A portion of the flow is contaminated with dye to visualize flow features. The channel employed is 1.59 cm thick, Reynolds numbers range from 10^0–10^1, and Richardson number ranges from 10^{-3}–2×10^1. A variety of flow features are evident in unstable, marginally stable and unstable flow domains, including streamwise vortices, hairpin vortices, spanwise structures, and localized turbulent motions. Spanwise and streamwise wave number variations in these structures are also described, along with the mixing onset boundary, and a scaling factor which accounts for the dependence of the mixing onset boundary on channel thickness.

Nomenclature

G gravitational acceleration
l' integral length scale characterizing vertical extent of mixing layer, equation (3)
Re Reynolds number, equation (2)
Ri Richardson number, equation (1)
s' channel streamwise coordinate measured from downstream edge of inlet splitter plate
u local streamwise velocity
U_c spatially-averaged velocity at bottom channel inlet or carrier substream
U_f spatially-averaged velocity at top channel inlet or feed substream
w channel thickness
x channel streamwise coordinate
y channel spanwise coordinate
z channel traverse coordinate.

Greek symbols
ΔU $U_c - U_f$
$\Delta\rho$ overall density difference between the feed and the carrier substreams, $\rho_f - \rho_c$
η fluid absolute viscosity
λ_{st} streamwise wave number
λ_{sp} spanwise wave number
$\bar{\rho}$ average density in the channel
ρ_c spatially-averaged density at bottom channel inlet or carrier substream
ρ_f spatially-averaged density at top channel inlet or feed substream.

1. Introduction

Existing investigations of the development of shear layers with density stratification focus on mixing and entrainment processes which occur in geophysical shear layers [1–5], the development and interaction of shear layer vortex structures [6–12], or combusting and react-

* Corresponding author

0017–9310/98 $19.00
PII: S0017–9310(98)00169–0

ing flows [13–17]. These investigations are conducted directly in the ocean or other large bodies of water [1–5], or using laboratory experiments which scale the geophysical and reacting/combusting flows [6–17]. In the latter case, free shear layers are generally produced in large open channels at high Reynolds numbers (i.e. from 10^2–10^3) with pressure gradients of approximately zero. The two streams producing the shear layer are most often arranged with globally stable density gradients such that heavier fluid is located beneath the lighter fluid. Results are applicable to climatology [1–12], ecosystem studies [1–12], pollutant dilution and dispersal [1–17], and non-premixed reactions and combustion [13–17].

Of the investigations with stable density stratification, Browand and Winant [6] and Koop and Browand [7] examine Kelvin–Helmholtz rollers, turbulence growth, and shear layer development at different Richardson numbers. A variety of events are observed, including relaminarization, interfacial waves, and a Holmboe mode of instability in high Richardson number shear layers. Brown and Roshko [8] examine relations between Kelvin–Helmholtz rollers and turbulence when density gradients are present. Patnaik et al. [9] investigate nonlinear shear layer development using two-dimensional numerical techniques. Alternations to Kelvin–Helmholtz roller cores and structures are observed as the Richardson number is altered. Staquet and Riley [10] describe three-dimensional numerical simulations of stratified shear layers. Klassen and Peltier [11] also use numerical schemes to provide information on the effects of Richardson number on shear layer stability and growth rates. Schowalter et al. [12] describe alterations to shear layer vortex structures from density stratification using numerical and experimental techniques. According to these investigators, buoyancy not only alters the evolution of the streamwise vortex tubes, but also induces the development of an additional collection of vortex structures.

Investigations of the development of streamwise and spanwise vortical structures in shear layers with no density stratification are more numerous. The most dominant feature of these flows, large-scale spanwise vortices often referred to as Kelvin–Helmholtz rollers, are reported for a wide range of Reynolds numbers [8, 18–20]. These vortices result from Kelvin–Helmholtz instabilities which arise when a region of strong shear is surrounded by a region of low shear. The instability and associated vortices are essential features of turbulent mixing layers, especially as they affect and control mixing layer dynamics. Organized streamwise structures superimposed on the spanwise vortical structures are also present in these mixing layers [21–26], and are included in numerous theoretical predictions of mixing layer development [27–30]. Both the streamwise vortex tubes and Kelvin–Helmholtz rollers are important in regard to mixing and entrainment between the two fluid streams in the mixing layers.

In contrast to other investigations of stably stratified shear layers [1–17] and shear layers without stratification [18–30], and with the exception of Ligrani et al. [31], our study is the first to examine the characteristics of instabilities from density stratification which is globally unstable in channel flows at very low Reynolds numbers. The unstable channel stratification is produced between two coincident streams of different velocity created using an inlet splitter plate, as illustrated in Fig. 1. Most previous laboratory investigations of shear layers [6–30] employ boundary layers just prior to shear layer formation, and uniform shear free flow with zero pressure gradient outside of the shear layers. Thus, the conditions for the development of Kelvin–Helmholtz instabilities are created. A streamwise pressure gradient is required in our enclosed channel. In addition, both entering streams in our study are duct flows before they reach the downstream end of the inlet splitter plate (just prior to initial shear layer formation) because of inlet passage

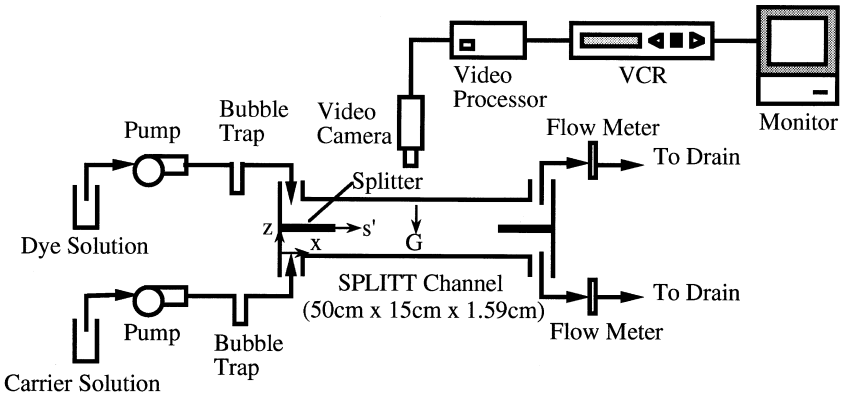

Fig. 1. Schematic of channel employed including apparatus used for flow visualization.

geometry. The presently employed channel is also relatively small, with a thickness w of 1.59 cm, breadth of 15 cm, and total length of 50 cm, giving an aspect ratio for each inlet of about 9.4. Consequently, Reynolds numbers here are less than two and thus, lower than values used in most other stratified shear layer studies [1–17]. Consequently, the present data cover experimental conditions not previously investigated thereby providing additional information on the relative importance of instabilities due to buoyancy and shear induced instabilities.

Results presented here are companion to data presented by Ligrani et al. [31]. In that paper, the mixing onset boundary separating flow development with and without significant mixing is determined in terms of a newly defined mixing onset parameter. This parameter depends upon the number and size distributions of polystyrene latex particles which enter through the top most inlet substream (relative to gravity) in a channel similar to the one shown in Fig. 1, and then leave the channel through one or two different exits. Thus, the polystyrene latex particles are used as flow tracers to give an indication of path line trajectories through the channel at different flow conditions. Flow mixing and entrainment are considered present when exiting particle size distributions are different from theoretically determined distributions [32] for two-dimensional, stable, laminar mass transfer in the channel. This theory predicts a particle size cut-off diameter resulting from the gravitational cross field which approximately separates larger sized particles which nominally leave the channel at the bottom exit from smaller sized particles which ordinarily leave the channel through the top exit [31, 32]. The present work is also applicable to mass transfer and fractionation of solid particles transported in liquid streams [31, 33].

In the present paper, the mixing onset boundary is again identified in terms of Richardson number, Reynolds number, and other flow parameters, but here this is accomplished from observations of flow visualization patterns using a dye which is initially inserted so that it contaminates the top most channel inlet stream. The 1.59-cm thick channel is sized and designed especially for visualization of flow characteristics over a range of Richardson numbers and Reynolds numbers to illustrate the nature of instabilities due to unstable density stratification at very low Reynolds numbers. The channel employed by Ligrani et al. [31] is 635 μm thick and thus 1/25 the size of the present channel making it too small to allow visualizations of flow details.

2. Experimental apparatus and procedures

2.1. The channel and experimental arrangement

The experimental setup used in this study is shown in Fig. 1. The channel employed is designed to split or separate two different flow streams using splitter plates oriented in x–y planes located at the channel inlet as well as at the channel exit. The channel is oriented so that gravity acts across the channel thickness. Channel surfaces are plexiglass. The thickness of each plexiglass splitter plate is 0.318 cm and the streamwise length into the channel is 15 cm. Each splitter plate extends across the entire breadth of the channel. Ends are machined flat with sharp corners. Each splitter plate and the two spacers which serve as side walls are sandwiched between two plexiglass pieces which serve as the channel top and bottom surfaces.

The channel inlets are supplied by two reservoirs 6000 ml (for the bottom inlet stream) and 2000 ml (for the top inlet stream) in size, which allow the facility to be operated continuously from 15–75 min. At the inlet, the splitter plate and channel walls provide a development length of 23.5 channel inlet widths or about 1 hydraulic diameter. The top inlet substream to the channel is pumped using a Fluid Metering Inc. QD0 pump, which provides 14–15 ml min^{-1} to the upper inlet. A Fluid Metering Inc. QD1 pump provides 80–400 ml min^{-1} to supply the bottom inlet.

2.2. Flow visualization apparatus

A Dage-MTI CCD72 camera and control box with a Computar Inc. 12.5 mm, F1.8 lens is connected to a Panasonic AG-1960 type 4-head, multiplex video cassette recorder, which is used to record the illuminated, time-varying patterns at rates as high as 30 frames per second. The 16.7 ms exposure time of the camera is set by its 60 Hz vertical sweep rate. Recorded images can be played back and photographed using the scan/stop action feature of this cassette recorder, and monitored using a Dage-MTI HR 1000 monitor. All measurements are made in a well lit room with extra lamps occasionally used to provide extra illumination of the visualized planes. The camera is positioned to capture views of flow visualization patterns in the streamwise/spanwise plane (or x–y plane) of the channel, as shown in Fig. 1, which also illustrates some of the components employed for the experiment. Images recorded on video tape (taken individually or in sequence) are then processed and digitized using Apple Video processing and capture software employed on a Macintosh Power PC computer. Images are then enhanced, further processed, and then arranged for printing using Adobe Photoshop software on the same computer.

2.3. Fluid stream characteristics

The fluid used at both channel inlets is distilled water. The dye is added to the top or feed substream to create an unstable density gradient at the location of the channel shear layer. The dye is also employed as a flow tracer

which follows flow path lines to indicate the existence, nature, and extent of channel secondary flows and mixing. The dye used in the solution is R250 Coomassie brilliant blue from Sigma Chemical Co. The Schmidt number of this dye in water is about 4200 indicating minimal dye diffusion. Similarly, the density of the feed (ρ_f) and/or carrier (ρ_c) substreams, and hence $\Delta\rho$, are modified by adding sucrose crystals dissolved in water to vary the degree of stratification between the two substreams. In the present study, the sucrose is added to the top inlet substream or feed substream to produce unstable stratification ($\rho_f > \rho_c, \Delta\rho > 0, Ri > 0$). The dye may also be added to the bottom inlet substream or carrier substream to produce stable stratification ($\rho_c > \rho_f$, $\Delta\rho < 0$, $Ri < 0$) [31]. Simple bubble traps are employed in each flow line leading to the channel to keep them free of bubbles.

2.4. Experimental conditions and procedure

Table 1 summarizes the experimental conditions employed. The velocity of the upper substream for all tests is 2.54×10^{-4} m s^{-1}. The velocity of the bottom inlet stream is changed to vary the Reynolds number from 10^0–10^1. The Richardson number is varied by either altering $\Delta\rho$, the density difference between the feed and carrier substreams or by varying ΔU, the average velocity difference between the carrier and the feed substreams. ΔU is set to a particular value by adjusting the stream velocity at the lower inlet. Spatially-averaged velocities in this inlet substream then range from 1.4×10^{-3} to 6.8×10^{-3} m s^{-1}. Richardson numbers then range from 10^{-3} to 2×10^1. Newly prepared feed and carrier solutions are employed for each subsequent test condition at a different $\Delta\rho$. All experiments are done at laboratory ambient temperature, which is usually approximately 24°C. Solution densities are also measured at 24°C using an AP Paar Corp. DMA model 602 high precision density meter, which gives values accurate to the sixth significant digit after the decimal in kg m^{-3}.

3. Experimental results

3.1. Characterization of channel behavior

The Richardson number and Reynolds number are used to quantify channel behavior. The form of the Richardson number employed here is the ratio of the square of the natural convection velocity scale to the square of the forced convection velocity scale. Following Schowalter et al. [12], the Richardson number is then given by

$$Ri = (\Delta\rho/\bar{\rho})Gl'/(\Delta U)^2. \tag{1}$$

The form of the Reynolds number employed here is given by

$$Re = \bar{\rho}\Delta U l'/\eta. \tag{2}$$

In both of these equations, l' represents the vertical thickness of the mixing layer. The equation used to evaluate the magnitudes of l' is given by Ligrani et al. [31] and similar in form to equations employed by Koop and Browand [7] and Schowalter et al. [12]

$$l' = \left(\frac{1}{\Delta U^2}\right)\int_{z_a}^{z_b}(u_c - u(z))(u(z) - u_f)\,dz. \tag{3}$$

Here, $u(z)$ is the local streamwise velocity at different channel traverse locations, just downstream of the inlet splitter plate, and u_c and u_f represent the local maximum magnitudes of the velocity distributions in the lower (carrier) and upper (feed) substreams, respectively. The limits of the integral, z_a and z_b, extend from one local velocity maximum to another.

To determine l', the mixing layer velocity profile $u(z)$ is numerically calculated at a location 20 mm downstream of the splitter plate using experimental flow conditions as input data for the FLUENT prediction code [31, 34]. The channel thickness and inlet splitter plate thickness employed in the FLUENT calculations are 1.59 and 0.318 cm, respectively. Inlet splitter plate length is 12.7 mm and the total channel length employed is 50 mm.

Table 1
Experimental conditions for flow visualization experiments

$U_c \times 10^3$ (m s^{-1})	$1'$ (μm)	$\Delta U \times 10^3$ (m s^{-1})	Re	Ri $\Delta\rho = 2.38$	$\Delta\rho = 1.24$	$\Delta\rho = 0.08$ (kg m^{-3})	$\Delta\rho = 0.03$	$\Delta\rho = 0.02$
1.4	996	1.15	1.14	17.63	9.16	0.59	0.253	0.126
2.45	906.7	2.2	2	4.38	2.28	0.15	0.063	0.031
3.5	858.4	3.25	2.79	1.90	0.99	0.06	0.027	0.013
4.5	857.2	4.25	3.63	1.11	0.58	0.04	0.016	0.008
5.8	854.2	5.52	4.71	0.66	0.34	0.02	0.009	
6.8	850.46	6.57	5.58	0.46	0.24	0.01	0.006	

Evaluated values of l', Re, and Ri, along with measured values of ΔU, U_c, and $\Delta\rho$ are tabulated in Table 1.

All data in Table 1 are obtained for $\Delta\rho > 0$ and $\rho_f > \rho_c$, or $Ri > 0$ which correspond to unstable density gradient conditions within the channel. Larger positive Richardson numbers thus indicate larger normalized magnitudes of the difference in density, $\Delta\rho = (\rho_f - \rho_c)$, between the upper feed substream and the lower carrier substream. As positive Richardson number increases, global and local density gradients across the mixing layer thus become more unstable. Note that the $\Delta\rho$ density difference is normalized by ΔU, the velocity difference between the two streams. Consequently, the Richardson number given by equation (1) can also be thought of as the normalized ratio of the density gradient (which drives the buoyancy instabilities) and the square of the overall velocity gradient (which provides a shear mechanism to induce flow instabilities). When $\rho_f < \rho_c$, stable density gradients are present across the mixing layer in the channel, $\Delta\rho < 0$, and the Richardson number is less than zero.

3.2. Mixing onset boundary

The mixing onset boundary from the $w = 635$ μm channel flow investigated by Ligrani et al. [31] is strongly dependent upon the magnitude of the Richardson number. As the Reynolds number increases from 0.3 to 1.1 in that study, the critical Richardson number at the mixing onset boundary varies between 0.0055 and 0.0010. Results which follow show the quantitative dependence on these parameters to be different in the 1.59 cm thick channel. Qualitative dependence is similar in that the flow generally becomes less stable as either the Richardson number and Reynolds number increases. As mentioned, the instability in Ligrani et al. [31] is quantified in terms of amounts of flow mixing and entrainment measured at the channel outlet. Here, unstable flow behavior is illustrated by specific visualized flow features which produce the same types of mixing and entrainment.

3.3. Flow characteristics at different Richardson numbers as the Reynolds number is held constant

Observations of visualized flow patterns at a fixed Reynolds number show a variety of different types of flow behavior as the Richardson number increases from zero. Some of these are illustrated in Fig. 2 at different $\Delta\rho$ and Ri for a Reynolds number of 2.79 as all channel flow rates are constant. At Richardson numbers less than 0.013, the dye in the streamwise/spanwise planes is uniform with almost no distortions or wrinkles along the entire length of the channel. Such behavior is shown for $Ri = 0.01$ at the bottom of Fig. 2. This figure also indicates that the image shown at this particular Richardson number is presented for a plane starting near $s' = 14$ cm. Each visualized image in Figs 2, 3, 5 and 6 shows the flow proceeding down the page.

As the Richardson number increases to $+0.03$, Fig. 2 shows that the dye becomes arranged into well defined longitudinal streaks as s' becomes greater than 6 cm. These streaks are believed to result from counter-rotating longitudinal vortices (with axes of vorticity in the streamwise direction) spread in an array across the channel span. The connection between flow visualization streaks and such vortices in unstratified shear layers is described by Lasheras and Choi [12] and Bernal [35]. Ligrani and Niver [36] also observe arrays of counter-rotating streamwise vortices associated with tubes of smoke which appear in plan views as elongated smoke lines. Similar observations are described by Matsson and Alfredsson [37]. In both of these cases, centrifugal instabilities are responsible for the development of the vortices in curved channels with large aspect ratios. The present flow visualization results are compared to ones from shear layers with no density stratification, shear layers with stable density stratification, and shear layers in other geometries because no other visualization results are known to be available from stratified mixing layers with globally unstable density gradients.

According to Lasheras, Cho, and Maxworthy [25], the streamwise vortices, in particular, make substantial contributions to the entrainment processes. The mixing and entrainment then disrupt mass transfer from that which exists when the channel flow is stable, laminar, and two-dimensional [31]. According to Konrad [38], mixing in unstratified shear layers is very small when it is dominated by molecular transport. When Reynolds number then increases to become greater than a critical value, a mixing transition takes place, and mixing is enhanced compared to nominal molecular levels. Gartrell [39] indicates that such bulk mixing is affected by fine-scale mixing layer structure and associated energy transfer, in addition to bulk flow characteristics.

A single spanwise wave length is associated with the vortex array for $Ri = 0.03$ in Fig. 2. A streamwise vortex structure with a single, well defined spanwise wavelength is also observed in free shear layers produced with splitter plates with sinusoidal spanwise forcing by Lasheras and Choi [26]. According to Lasheras et al. [25], such streamwise vortices contribute substantially to the entrainment processes between the two streams. Thus, they are expected to lead to the redistributions of polystyrene latex particles observed by Ligrani et al. [31], which are indicated to occur when local flow behavior deviates from stable, laminar, two-dimensional behavior.

According to Lin and Corcos [29] and Lasheras and Choi [26], after such vortices are enhanced by stretching with no density stratification, the vorticity is pulled more strongly in the streamwise direction until a series of hairpin vortex structures form. These form around fluid containing significant spanwise vorticity associated with

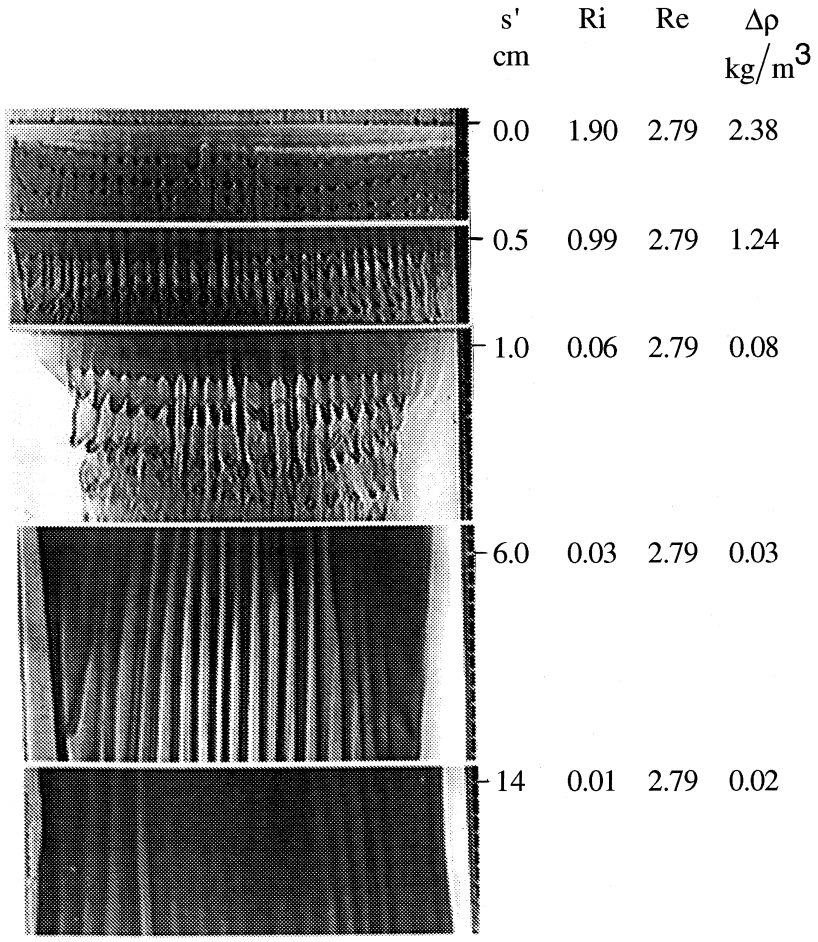

Fig. 2. Flow patterns at $Re = 2.78$ visualized in streamwise/spanwise planes at different Richardson numbers.

Kelvin–Helmholtz rollers, and extend from the underside of one roller to the top of the neighboring roller. They indicate that the distortion of the spanwise braid of vorticity is 180° out of phase with the distortion of the vortex cores. The results in Fig. 2 for a Richardson number of 0.06 indicate that something similar may be happening in the present study. This is particularly interesting since our Reynolds numbers are quite low (<2) resulting in very weak shear layers, and since our overall density gradients are unstable. Consequently, the formation sequence of the Kelvin–Helmholtz spanwise vortices are probably different than in stably stratified and unstratified shear layers which develop at much higher Reynolds numbers. According to Ligrani et al. [31], if the Kelvin–Helmholtz rollers do exist at Reynolds numbers less than two, they are probably triggered or initiated in some way by the disturbances induced by unstable density stratification. Alternatively, if the Kelvin–Helmholtz vortex structures ordinarily present at higher Reynolds numbers are not present in our channel, then the observed vortex structures and associated mixing and entrainment then result entirely from unstable density stratification alone.

In Fig. 2, the results observed just downstream of $s' = 1.0$ cm at $Ri = 0.06$ show small structures across the span of the channel which clearly have a hairpin structure and appearance. These are spread across the channel span in several different arrays located at different streamwise locations. Spanwise variations of dye concentration are also present between adjacent hairpin structures. As the flow advects downstream, the hairpin vortices become smaller and less well defined, sometimes taking the forms of small loops of dye. Some break up of all of these dye forms seems to occur at the downstream end of the $Ri = 0.06$ image in Fig. 2.

Qualitatively similar behavior is evident for Ri of 0.99 and 1.90 in Fig. 2 which are also given for $Re = 2.79$. Compared to the $Ri = 0.06$ results, the dye patterns at these two higher Richardson numbers show hairpin vortex arrays which occur closer to the downstream end of the splitter plate where $s' = 0$. The spatial extents and

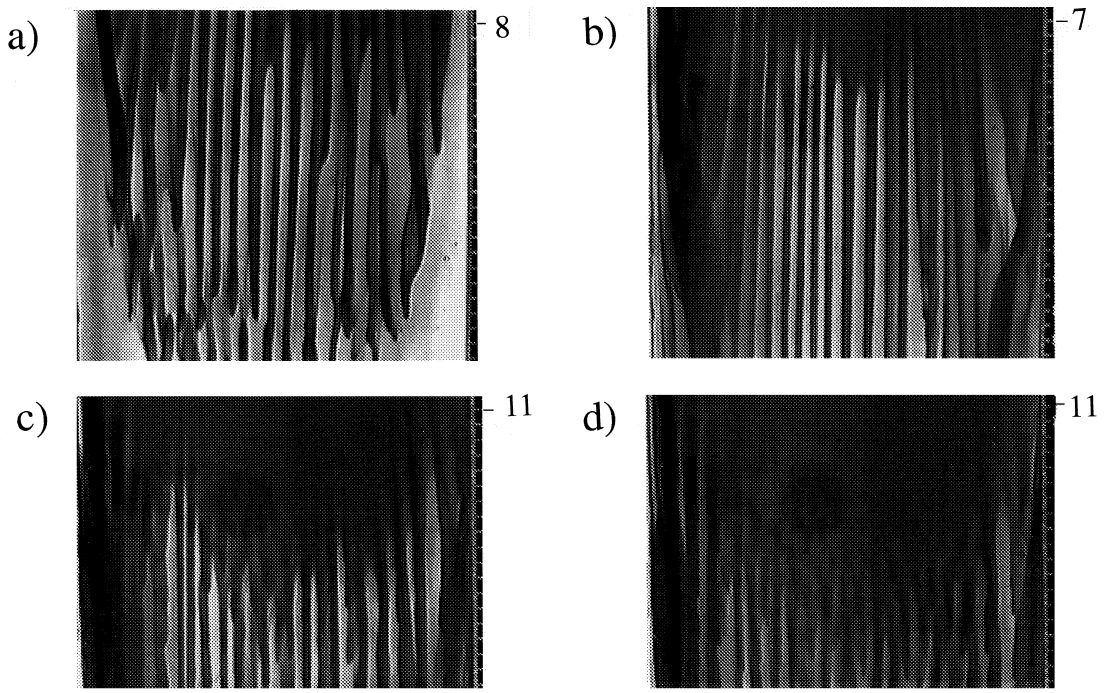

Fig. 3. Flow patterns at $Re = 2.00$ visualized in streamwise/spanwise planes at different channel locations and at different times relative to dye injection illustrating marginally stable channel behavior. Times after start of dye injection for flow visualization sequence: (a) 0.5 min; (b) 2.0 min; (c) 7.0 min; (d) 10.0 min.

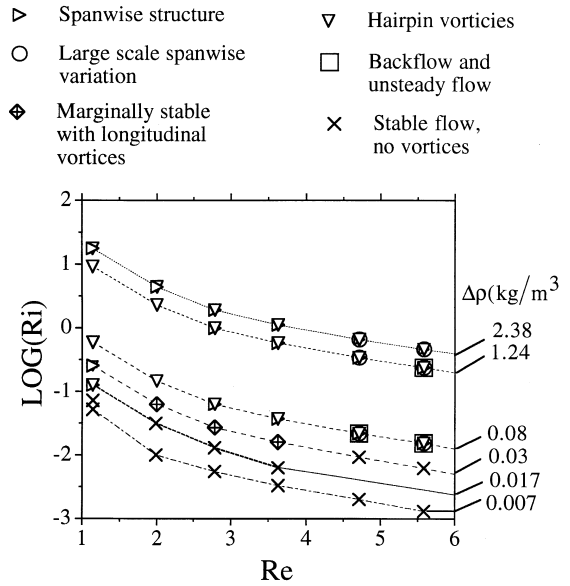

Fig. 4. Experimental domain map illustrating types of observed dye patterns at different Reynolds numbers and different Richardson numbers.

amounts of dye distortion are generally present further upstream as the Richardson number increases. In addition, the vortices at Ri of 0.99 and 1.90 are smaller and closer together in both the spanwise and streamwise directions compared to the $Ri = 0.06$ patterns (noting that the scale sizes in each image are about the same). Thus, streamwise and spanwise wave numbers associated with these vortex structures seem to increase with Richardson number as the Reynolds numbers is held constant.

Similar trends are observed at all other Reynolds numbers examined, except at the lowest Reynolds number investigated, 1.1. At this condition, the channel flow is very sensitive to minor disturbances and the onset of the instabilities in the channel flow is rather unpredictable. Consequently, trends of visualized flow patterns at $Re = 1.1$ are somewhat different from trends observed at higher Reynolds numbers.

3.4. Marginally stable behavior

A sequence of dye images which have qualitative behavior similar to the $Ri = 0.03$, $Re = 2.79$ image in Fig. 2 are presented in Fig. 3. These images are obtained at $Re = 2.00$ and $Ri = 0.08$ at different times and different

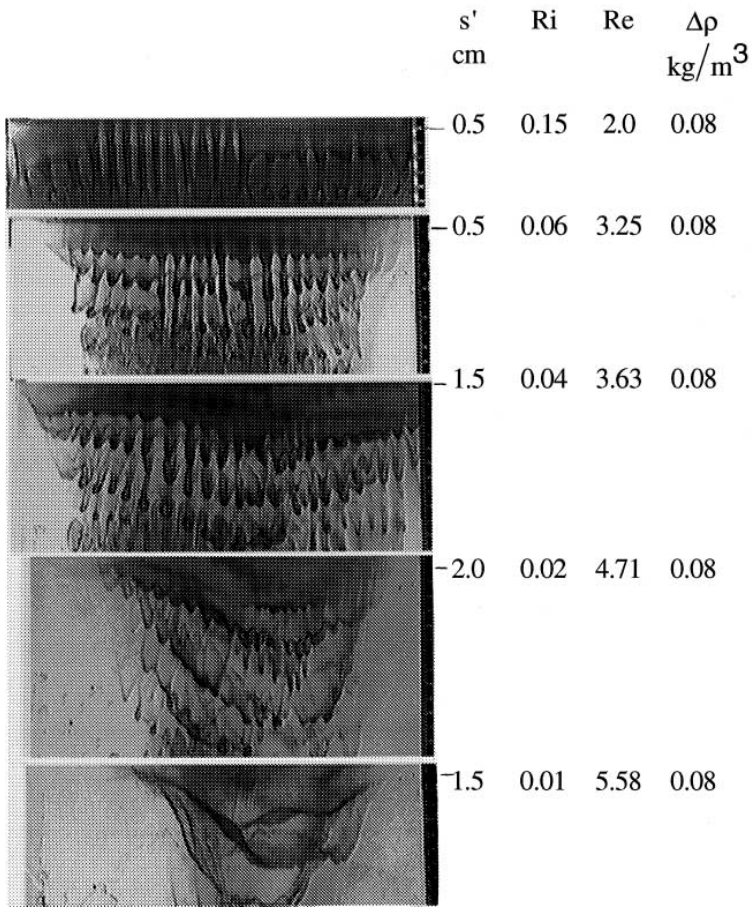

Fig. 5. Flow patterns at $\Delta\rho = 0.08$ kg m^{-3} visualized in streamwise/spanwise planes at different Richardson numbers and different Reynolds numbers.

channel streamwise locations as the distorted dye images are advected through the channel. The dye pattern initially present in Fig. 3(a) at $s' = 8$ cm and just downstream is typical of dye patterns formed by an array of longitudinal vortices in the channel. Note that individual vortex pairs occasionally wrap around each other. Splitting and merging of vortex pairs is also evidenced by strips of dye which merge together and split apart as they are advected downstream. Such splitting and merging of vortex pairs is also observed in arrays of Gortler vortices in curved boundary layers, and in arrays of Dean vortices in curved channels [36, 37, 40].

As the distorted dye images advect downstream, Figs 3(b), (c) and (d) indicate that the streamwise vortex arrays associated with them are present at farther downstream locations as the channel operates. Upstream of these locations, the dye layer is uniform without appreciable distortions indicating locally stable flow behavior. Thus, the instabilities at this experimental condition are transitory. Longitudinal vortices which are initially present just downstream of the inlet splitter plate gradually shift towards the outlet end of the channel to eventually disappear as time increases. Such flow behavior is thus characterized as marginally stable. Features observed in the dye patterns seem to be triggered by some disturbance which is present in the channel only initially and temporarily. The most likely event producing such behavior is associated with pump start-up and the transients which follow. Thus, the only instabilities evident in Fig. 3 are present temporarily only as they continue to be triggered by small scale disturbances present near the channel inlet.

3.5. Experimental domain map of flow features

Results such as the ones shown in Figs 2 and 3 are used to create the experimental domain map presented in Fig. 4. This figure is a compilation of all of our data, and as such, shows the types of flow structures from observed dye patterns at different experimental conditions. These are presented in the figure for different

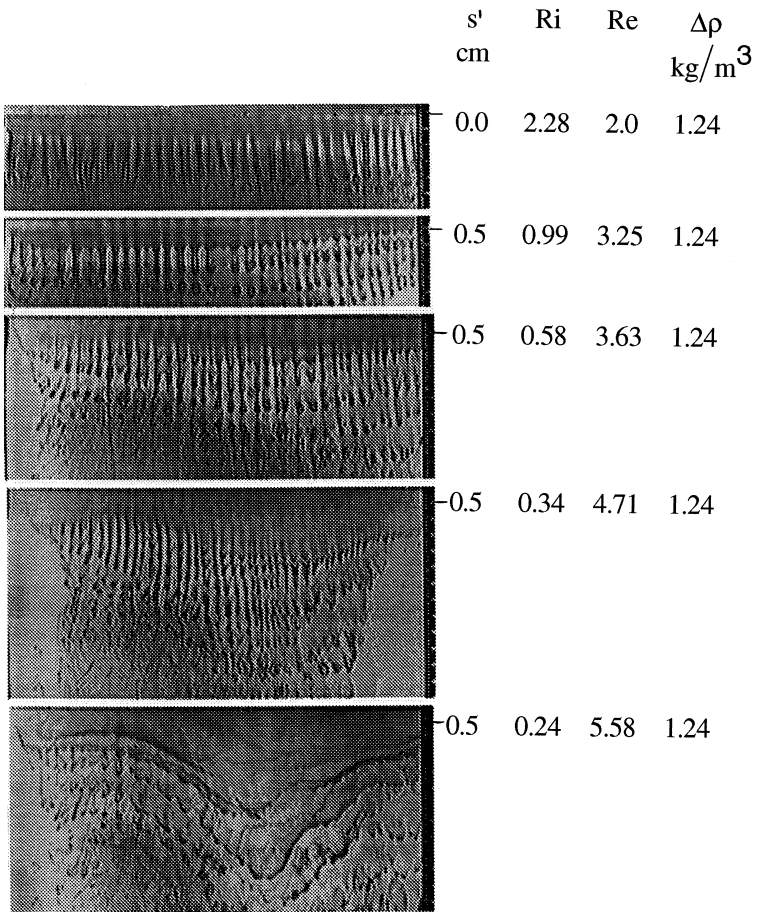

Fig. 6. Flow patterns at $\Delta\rho = 1.24$ kg m^{-3} visualized in streamwise/spanwise planes at different Richardson numbers and different Reynolds numbers.

values of the Richardson number, Reynolds number, and overall density difference $\Delta\rho$, which ranges from $+0.007$ to $+2.38$ kg m^{-3}. Each vertical column of data is obtained at the same Reynolds number. Lines of positive constant $\Delta\rho$ are also indicated in the figure. A different symbol is used to label each observed flow feature.

Figure 4 shows that stable, unmixed flow with no vortices in present in the channel at all Reynolds numbers investigated provided the Richardson number is less than $10^{-1.5}$–10^{-1}. Stable flow is characterized by uniform sheets of dye with approximately straight smooth edges and almost no convolutions or variations, as mentioned. As the Richardson number then increases at any particular value of the Reynolds number, the flow becomes marginally stable and longitudinal flow features such as the ones in Fig. 2 for $Ri = 0.03$ and in Fig. 3 are present. The Richardson number value at any particular Reynolds number just below this 'marginally stable with longitudinal vortices' boundary are higher than Ri values corresponding to the mixing onset boundary in the 635 μm thick channel investigated by Ligrani et al. [31]. There, Re and Ri at the mixing onset boundary range from 10^{-1} to 10^{0} and from 10^{-3} to 10^{-2}, respectively.

Events observed in the 1.59 cm thick channel at Richardson numbers (at a particular Re) higher than ones corresponding to the marginally stable regime are considered to be unstable with mixing [31]. In the flow domain with mixing, Fig. 4 indicates that the visualizations show hairpin vortices, spanwise structures, large scale spanwise variations, and back flow and large-scale unsteady flow. The hairpin vortices are almost always preceded or accompanied by longitudinal vortices. The flow visualization images for $Re = 2.79$ and Ri of 0.06, 0.99 and 1.90 in Fig. 2 are typical of dye patterns with hairpin vortices and spanwise flow structures. As the Reynolds number increases to become greater than 4.5 at a given value of $\Delta\rho$, Fig. 4 indicates that dye patterns with large-scale spanwise structures and/or back flow and unsteady flow are present in the channel, provided $\Delta\rho$ is 0.08 kg m^{-3} or greater.

3.6. Flow characteristics at different Richardson numbers and Reynolds numbers as the overall density gradient is held constant

Visualized flow patterns which illustrate flows with hairpin vortices, small- and large-scale spanwise structures, back flow, and large-scale unsteady flow in combination are presented in Figs 5 and 6. The results in Fig. 5 are given for $\Delta\rho = +0.08$ kg m^{-3} and the ones in Fig. 6 represent $\Delta\rho = +1.24$ kg m^{-3}. Thus, the data sequence in each of these figures follows a negatively sloped line of constant $\Delta\rho$ in Fig. 4. In each case, the Reynolds number and Richardson number are altered by varying the carrier substream flow rate as positive $\Delta\rho$ is maintained constant.

All experimental conditions represented by the images in Figs 5 and 6 correspond to unstable flow with mixing. Hairpin vortex structures are evident for each *Re*, *Ri*, and $\Delta\rho$ shown. At $Re = 2.0$ in Fig. 5, the hairpin vortices and longitudinal streaks of dye which accompany them are the only features evident. At *Re* of 3.25 and 3.63, the dye patterns additionally show wavy horizontal lines at different streamwise locations, which result from some sort of spanwise structures. When such structures are present, the hairpin vortices sometimes seem to dissociate from the upstream located longitudinal vortex structures and then appear as small, oval-shaped loops of dye. As the Reynolds number reaches 4.71 and 5.58, Fig. 5 shows large-scale spanwise variations of dye. Occasional regions of locally augmented unsteadiness and reversed flow (occurring in the negative *x*-direction as back flow) are also present, which are most evident as corresponding video images are viewed to change with time.

The evolution of streamwise vortex tubes into hairpin vortices and then into small, oval loops of vorticity, illustrated at certain conditions in Figs 5 and 6, is probably due to interactions between the streamwise vortex tubes and the spanwise structures in the flow. However, the types and character of the vortical events which are responsible for the spanwise structures are not clear from the present results. When Kelvin–Helmholtz rollers are present at much higher Reynolds numbers in flows with no stratification or stable stratification [8, 12, 18–20], the hairpin vortices form by themselves, or as vortex tubes are wrapped around the larger spanwise roller structures. According to Lasheras and Choi [26] the development of the streamwise vortex tubes is connected to the amplification of perturbations in spanwise vorticity. The vortex structures with spanwise and streamwise axes then interact by rolling around each other [6]. As this occurs, the tubes can be placed over and beneath the rollers [12]. In some cases, the thin vortex tubes between the vortex roller cores are eventually wrapped around them over the top of one roller and then beneath an adjacent roller. When such observations from other shear layers at higher Reynolds numbers, both with and without stable density stratification [6–30], are compared to the images in Figs 2, 5 and 6 obtained with unstable density stratification, important similarities are thus evident.

Important differences are also apparent. This is true if one considers the development of hairpin vortices, which seem to be somewhat more abundant in the unstably stratified shear layers examined in our investigation. By comparing Figs 5 and 6 to Fig. 25 from Schowalter et al. [12], it is also evident that the interactions between streamwise vortices and spanwise flow structures are significantly different. In Schowalter et al. [12], fluid with higher density from the lower stream is entrained by the vortex core and pulled over the top of it. The concentrated vorticity in the Kelvin–Helmholtz rollers thus carries heavy fluid above the light fluid. Additional vortices then result from such events because of the baroclinic production term in the variable density vorticity transport equation [12]. The resulting vortices are substantially different from the streamwise vortices ordinarily generated in mixing layers with no density stratification. Density stratification also results in complicated variations of the wrapping of the streamwise vortex tubes around spanwise vortex structures, which often produces streamwise vortex tubes with widely different appearances. The developing streamwise vortex structures in the present study provide additional variations of vortex structure because both local and global density gradients are unstable, and because shear layers are considerably weaker.

In shear layers with no density stratification, Kelvin–Helmholtz instabilities are generally present when Reynolds numbers are greater than 30–35 [41]. Our Reynolds number range is considerably lower, from 10^0 to 10^1, resulting in much weaker shear layers. Thus, the spanwise structures evident in Figs 5 and 6 are believed to be due to Kelvin–Helmholtz rollers only if the Kelvin–Helmholtz instabilities are initiated in some way by the locally unstable density gradients, as mentioned. A more likely explanation is that the flow structures evident in Figs 2, 3, 5, and 6 are more a result of unstable density stratification and Rayleigh–Bernard type instabilities, than from instabilities due to shear and the Kelvin–Helmholtz mechanism.

Results in Fig. 6 for $\Delta\rho = +1.24$ kg m^{-3} show many qualitative similarities and differences compared to the results in Fig. 5 for $\Delta\rho = +0.08$ kg m^{-3}. Both figures show unstable flow features which begin to develop close to the downstream edge of the splitter plate, and then propagate further downstream both as the Reynolds number increases and as the Richardson number decreases. Results obtained at the higher Reynolds numbers show spanwise disturbances which dominate the flow and produce continuous changes in the dye patterns. Hairpin vortex structure is different in Figs 5 and 6 since sizes decrease, and spanwise spacings between adjacent hairpins are smaller giving higher spanwise wave numbers at the higher positive $\Delta\rho$. Another interesting differ-

ence is evident if the $\Delta\rho = +0.08$ kg m^{-3} $Re = 5.58$ results in Fig. 5 are compared to the $\Delta\rho = +1.24$ kg m^{-3} $Re = 5.58$ results in Fig. 6. In the latter figure, more numerous hairpin-like vortices are evident in the channel which are superimposed on the large-scale spanwise variations of dye. All of these different modes of behavior produce significant mixing and entrainment between the two fluid streams.

3.7. Streamwise and spanwise wave number variations

Streamwise and spanwise wave number variations are presented in Figs 7 and 8. Such data reveal important aspects of vortex structure spacings and development as the Reynolds number, Richardson number, and overall density gradient vary. Wave numbers are determined from measurements of spacings between vortex structures in the streamwise and spanwise directions.

The variations of the dimensional streamwise wave number and dimensional spanwise wave number at constant Reynolds number as the Richardson number varies are shown in Fig. 7 for Re of 1.14, 2.0, 2.78, 3.63, 4.71, and 5.52. Streamwise wave numbers in the top portion

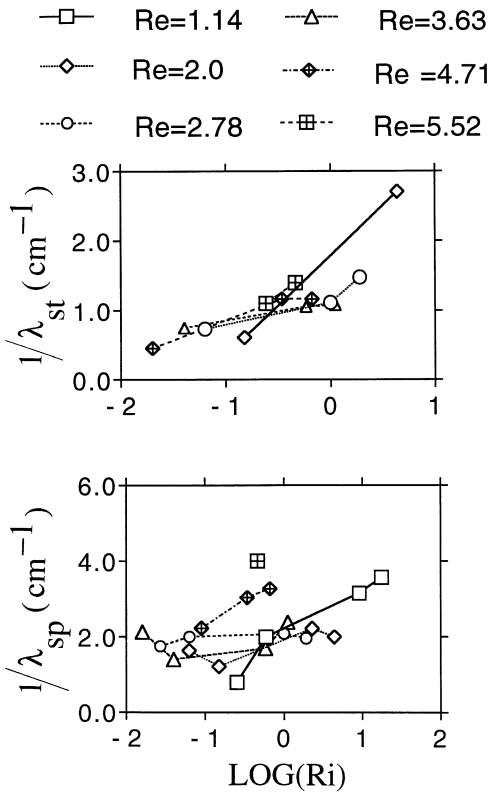

Fig. 7. Dimensional wave numbers as dependent upon Reynolds number and Richardson number. (a) Streamwise wave number. (b) Spanwise wave number.

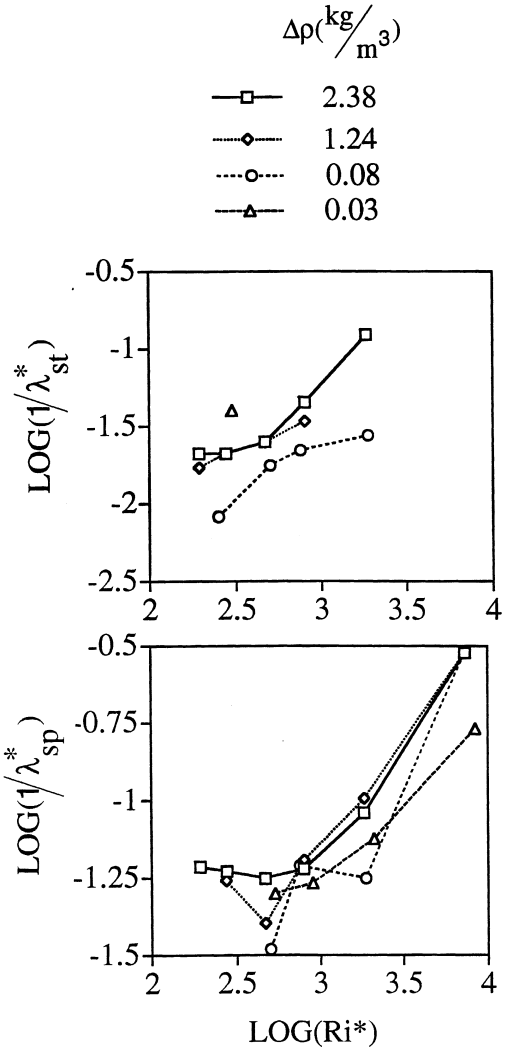

Fig. 8. Non-dimensional wave numbers as dependent upon Reynolds number and Richardson number. (a) Streamwise wave number. (b) Spanwise wave number.

of the figure generally increase with Ri at each value of Re. This evidences vortex structures which are smaller and closer spaced as the Richardson number increases. The streamwise wave number is approximately equal to 0.5 cm^{-1} when the flow in marginally stable and arrays of longitudinal vortices are present in the channel shear layer. Another interesting feature of the dimensional streamwise wave number data at different Re is their grouping together into one broad curve.

Spanwise wave numbers in the bottom portion of Fig. 7 either remain about constant or increase as the Richardson increases at constant Reynolds number. The $1/\lambda_{sp}$ data range from 0.5 to 4.0 cm^{-1} as Re and Ri vary, and thus do not collapse onto a single curve.

The data in Fig. 7 are also presented in Fig. 8 in non-dimensional form. In Fig. 8, the data are presented as dependent upon the Richardson number as the overall positive density gradient $\Delta\rho$ is held constant for $\Delta\rho$ of $+0.03\ \mathrm{kg\ m^{-3}}$, $+0.08\ \mathrm{kg\ m^{-3}}$, $+1.24\ \mathrm{kg\ m^{-3}}$ and $+2.38\ \mathrm{kg\ m^{-3}}$. Ri^* is employed on the abscissa of the two plots in Fig. 8. This quantity is given by

$$Ri^* = Ri(\bar{\rho}/\Delta\rho) \tag{4}$$

which is the same as

$$Ri^* = Gl'/(\Delta U)^2. \tag{5}$$

The normalized forms of the streamwise and spanwise wave numbers employed along the ordinate axes in Fig. 8 are, respectively, expressed as

$$1/\lambda^*_{sp} = l'/\lambda_{sp}\,Re \quad \text{and} \quad 1/\lambda^*_{st} = l'/\lambda_{st}\,Re. \tag{6,7}$$

These are then equivalent to

$$1/\lambda^*_{sp} = \eta/\lambda_{sp}\bar{\rho}(\Delta U) \quad \text{and} \quad 1/\lambda^*_{st} = \eta/\lambda_{st}\bar{\rho}(\Delta U) \tag{7,8}$$

respectively. With this plotting scheme, Fig. 8 shows that the normalized streamwise and spanwise wave numbers both generally increase with Ri^* as $\Delta\rho$ is held constant. The normalized spanwise data for different $\Delta\rho$ in the bottom portion of the figure approximately collapse together in one broad curve. The streamwise wave number data in the top portion of Fig. 8 show increasing $1/\lambda^*_{st}$ with $\Delta\rho$ at each Ri^*, except for one data point associated with $\Delta\rho = +0.03\ \mathrm{kg\ m^{-3}}$. This exceptional behavior is probably due to occasional effects of the channel side walls on the uniformity of the vortices across the measurement plane.

3.8. More on the mixing onset boundary

The mixing onset boundary determined from the present flow visualization results is compared to the mixing onset boundary determined by Ligrani et al. [31] in a smaller, 635 μm thick channel in Fig. 9. The mixing onset boundaries from the two channels occur over different ranges of Reynolds number and Richardson number. These differences are due to different channel thicknesses, and to different shear layer initial profiles and conditions at the downstream edges of the inlet splitter plates. In both cases, the channel flow becomes more unstable either as the Reynolds number increases or as the Richardson increases. Another interesting feature of the data is the fact that stable behavior with no mixing is present in the channel shear layer at lower values of the Richardson number, regardless of the magnitude of the Reynolds number. Our Reynolds numbers range from 10^0 to 10^1 which are significantly lower than values employed by Browand and Winant [6], Koop and Browand [7] and Showalter et al. [12]. Our Richardson numbers range from 10^{-3} to 2×10^1 and thus include the ranges of values covered in these other studies.

The data from Fig. 9 are also plotted in Fig. 10. In this

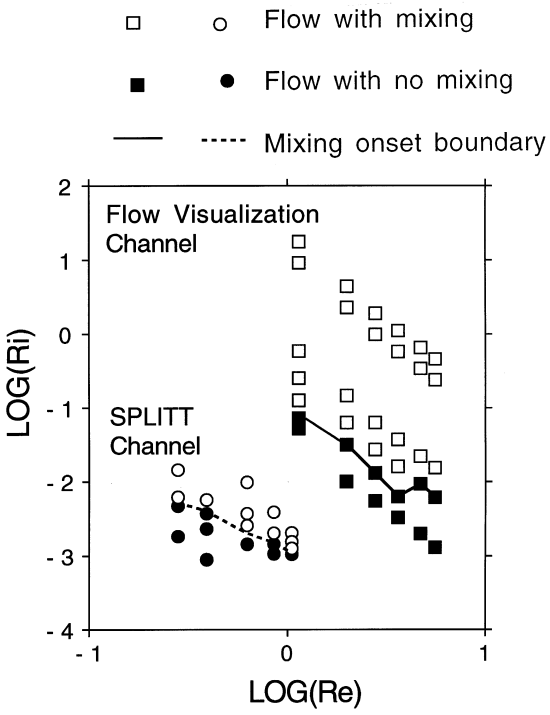

Fig. 9. Mixing onset boundaries from flow visualization channel and from a 635 μm thick SPLITT channel as dependent upon Richardson number and Reynolds number.

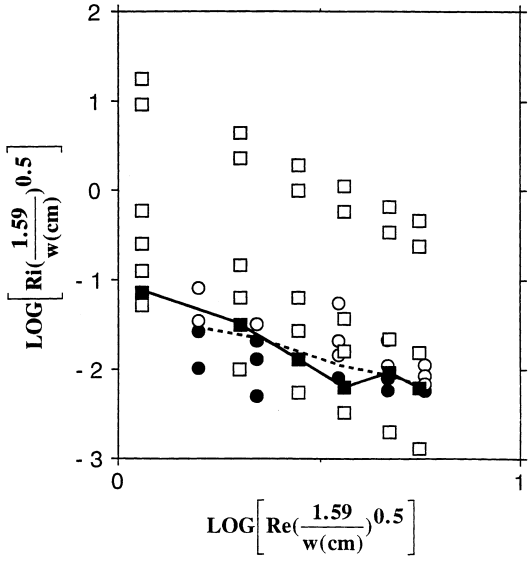

Fig. 10. Mixing onset boundaries from flow visualization channel and from a 635 μm thick SPLITT channel as dependent upon Richardson number and Reynolds number, after scaling to account for differences in channel sizes. Symbols are the same as employed in Fig. 9.

case, the data are again given as they are dependent upon Reynolds number and Richardson number, but here, the Reynolds number and Richardson number are multiplied by the scaling factor $(1.59/w)^{0.5}$ (where w is given in centimeters, and the 1.59 number in the factor represents the thickness of the larger channel in centimeters) to account for differences in channel thicknesses. Figure 10 shows that this approach causes the mixing onset boundaries from the two different experiments to coincide and to show similar quantitative dependence on Re and Ri.

4. Summary and conclusions

Characteristics of flow instabilities in a shear layer with globally unstable density stratification are examined in a 1.59 cm thick rectangular channel at low Reynolds numbers ($Re < 10$) and Richardson numbers from 10^{-3} to 2×10^{1}. Stable, marginally stable, and unstable flow features are discerned after one inlet substream is contaminated with dye. The unstable and stable flow regimes are associated with and without substantial channel mixing, respectively.

A variety of flow features are evident in the unstable and marginally stable flow domains, including streamwise vortices, hairpin vortices, spanwise structures, and localized turbulent motions. Streamwise wave numbers within the unstable flow structures decreases as the Richardson number decreases and the mixing onset boundary is approached. No distortions of the dye patterns, indicating minimal channel secondary flows, are observed in the stable flow domain. Temporarily present longitudinal streaks of dye, which evidence transitory longitudinal vortices, are observed in a marginally stable flow regime. The presence and development of these different vortical flow structures are significant because: (i) they increase channel mixing and entrainment between the two channel substreams thereby altering mass transfer from that which exists when channel flow is laminar, stable, and two-dimensional [31] and (ii) they are believed to result more from unstable density stratification and Rayleigh–Bernard type instabilities, than from instabilities due to shear and the Kelvin–Helmholtz mechanism.

Experimental conditions at the mixing onset boundary separating flow regimes with and without substantial mixing are identified and compared to ones observed in a channel with a thickness of 635 μm [31]. A scaling factor, based on the square root of the ratio of channel thicknesses, is applied to the Reynolds number and Richardson number to account for the dependence of the mixing onset boundary on channel size. With this information, mixing onset boundary characteristics of stratified shear layers in other applications can be determined when initial conditions and boundary conditions are similar.

Acknowledgements

The authors acknowledge support for this project from NSF Grant No. CHE-9322472. Dr M. N. Myers and Professor K. Caldwell are also acknowledged for their assistance with the experimental apparatus and facilities.

References

[1] J.D. Woods, Wave-induced shear instability in the summer thermocline, Journal of Fluid Mechanics 32 (1968) 791–800.
[2] I. Orlanski, K. Bryan, Formulation of the thermocline step structure by large amplitude internal gravity waves, Journal of Geophysical Research 74 (1969) 6975–6983.
[3] G.O. Marmorino, Observations of small-scale mixing processes in the seasonal thermocline, Part II: wave breaking, Journal of Physical Oceanography 17 (1987) 1348–1355.
[4] S.A. Thorpe, A.J. Hall, C. Taylor, J. Allen, Billows in Loch Ness, Deep-Sea Research 24 (1977) 371–379.
[5] D.M. Farmer, L. Armi, The flow of Atlantic water through the Strait of Gibralter, Progress in Oceanography 21 (1988) 1–8.
[6] F.K. Browand, C.D. Winant, Laboratory observations of shear-layer instability in a stratified fluid, Boundary Layer Meteorology 5 (1973) 67–77.
[7] C.G. Koop, F.K. Browand, Instability and turbulence in a stratified fluid with shear, Journal of Fluid Mechanics 93 (1979) 135–159.
[8] G.L. Brown, A. Roshko, On density effects and large structure in turbulent mixing layers, Journal of Fluid Mechanics 64 (1974) 775–816.
[9] P.C. Patnaik, F.S. Sherman, G.M. Corcos, A numerical simulation of Kelvin–Helmholtz waves of finite amplitude, Journal of Fluid Mechanics 73 (1976) 215–240.
[10] C. Staquet, J.J. Riley, On the velocity field associated with potential vorticity, Dynamics Atmospheres and Oceans 14 (1989) 93–123.
[11] G.P. Klassen, W.R. Peltier, The influence of stratification on secondary instability in free shear layers, Journal of Fluid Mechanics 227 (1991) 71–106.
[12] D.S. Schowalter, C.W. Van Atta, J.C. Lasheras, A study of streamwise vortex structure in a stratified shear layer, Journal of Fluid Mechanics 281 (1994) 247–291.
[13] S. Komori, T. Kanzaki, Y. Murakami, Simultaneous measurements of instantaneous concentrations of two species being mixed in a turbulent flow by using a combined laser-induced fluorescence and laser-scattering technique, Physics of Fluids A 1 (2) (1989) 349–352.
[14] S. Komori, J.C.R. Hunt, T. Kanzaki, Y. Murakami, The effects of turbulent mixing on the correlation between two species and on concentration fluctuations in non-premixed reacting flows, Journal of Fluid Mechanics 228 (1991) 629–659.
[15] K. Nagata, S. Komori, Heat and mass transfer in strong stratification, Transactions of the Japan Society of Mechanical Engineers B 61 (586) (1995) 2197–2205.
[16] K. Nagata, S. Komori, Direct numerical simulation of the Prandtl number effects on the counter-gradient scalar trans-

fer in strong stable stratification, Transactions of the Japan Society of Mechanical Engineers B 62 (600) (1996) 3142–3148.
[17] S. Komori, K. Nagata, Effects of molecular diffusivities on counter-gradient scalar and momentum transfer in strong stable stratification, Journal of Fluid Mechanics 326 (1996) 205–237.
[18] H.W. Liepmann, J. Laufer, Investigation of free turbulent mixing, NACA Technical Note 1257, 1947.
[19] M. Rebollo, Analytical and experimental investigation of turbulent mixing layer of different gases in a pressure gradient, Ph.D. thesis, California Institute of Technology, Pasadena, CA, 1973.
[20] P. Dimotakis, G.L. Brown, The mixing layer at high Reynolds number: large structure dynamics and entrainment, Journal of Fluid Mechanics 78 (1976) 535–560.
[21] R.E. Breidenthal, Structure in turbulent mixing layers and wakes using a chemical reaction, Journal of Fluid Mechanics 97 (1981) 771–781.
[22] L.P. Bernal, A. Roshko, On density effects and large structure in turbulent mixing layers, Journal of Fluid Mechanics 64 (1974) 775–816.
[23] J. Jimenez, A spanwise structure in the shear layer, Journal of Fluid Mechanics 132 (1983) 319–336.
[24] J. Jimenez, M. Cogollos, L.P. Bernal, A perspective view of the plane mixing layer, Journal of Fluid Mechanics 152 (1985) 125–143.
[25] J.C. Lasheras, J.S. Cho, T.M. Maxworthy, On the origin and evolution of streamwise vortical structures in a plane free shear layer, Journal of Fluid Mechanics 172 (1986) 231–258.
[26] J.C. Lasheras, H. Choi, Three-dimensional instability of a plane free shear layer: an experimental study of the formation and evolution of streamwise vortices, Journal of Fluid Mechanics 189 (1988) 53–86.
[27] G.M. Corcos, The mixing layer: deterministic models of a turbulent flow, Mechanical Engineering Report FM-79-2, University of California at Berkeley, Berkeley, CA, 1979.
[28] R.T. Pierrehumbert, S.E. Widnall, The two- and three-dimensional instabilities of a spatially periodic shear layer, J. Fluid Mechanics 114 (1982) 59–82.
[29] S.J. Lin, J.M. Corcos, The mixing layer: deterministic models of a turbulent flow. Part 3. The effect of plane strain on the dynamics of the streamwise vortices, Journal of Fluid Mechanics 141 (1984) 139–178.
[30] G.M. Corcos, S.J. Lin, The mixing layer: deterministic models of a turbulent flow. Part 2. The origin of the three dimensional motion, Journal of Fluid Mechanics 139 (1984) 67–95.
[31] P.M. Ligrani, S. Gupta, J.C. Giddings, Onset and effects of instabilities from unstable stratification of density on mass transfer in channel shear layers at low Reynolds numbers, International Journal of Heat and Mass Transfer 41 (1998) 1667–1679.
[32] J.C. Giddings, Optimization of transport-driven continuous SPLITT fractionation, Separation Science and Technology 27 (1992) 1489–1504.
[33] S. Gupta, Investigations of resolution deteriorating factors and new applications in continuous SPLITT fractionation, Ph.D. thesis, University of Utah, Salt Lake City, UT, 1997.
[34] FLUENT (V4), Version 4.2, Fluent Inc., Lebanon, New Hampshire, 1993.
[35] L.P. Bernal, The coherent structure of turbulent mixing layers, Ph.D. thesis, California Institute of Technology, Pasadena, CA, 1981.
[36] P.M. Ligrani, R.D. Niver, Flow visualization of Dean vortices in a curved channel with 40:1 aspect ratio, Physics of Fluids 31 (12) (1988) 3605–3617.
[37] O.J.E. Matsson, P.H. Alfredsson, Curvature- and rotation-induced instabilities in channel flow, Journal of Fluid Mechanics 210 (1990) 537–563.
[38] J.H. Konrad, An experimental investigation of mixing in two-dimensional turbulent shear flows with application to diffusion-limited chemical reactions, Project SQUID Tech. Rep. CIT-8-PU, 1976.
[39] G. Gartrell, Studies on the mixing in a density-stratified shear flow, Ph.D. thesis, California Institute of Technology, Pasadena, CA, 1979.
[40] P.M. Ligrani, J.E. Longest, M.R. Kendall, W.A. Fields, Splitting, merging and spanwise wave number selection of Dean vortex pairs, Experiments in Fluids 18 (1) (1994) 41–58.
[41] P. Dimotakis, Private communication, 1996.